Development of a Mars lidar (MARLI) for measuring wind and aerosol profiles from orbit

Daniel R. Cremons, James Abshire, Graham Allan, Xiaoli Sun, Haris Riris, et al.

Daniel R. Cremons, James Abshire, Graham Allan, Xiaoli Sun, Haris Riris, Michael Smith, Scott Guzewich, Anthony Yu, Floyd Hovis, "Development of a Mars lidar (MARLI) for measuring wind and aerosol profiles from orbit," Proc. SPIE 10791, Lidar Technologies, Techniques, and Measurements for Atmospheric Remote Sensing XIV, 1079106 (9 October 2018); doi: 10.1117/12.2325408

SPIE.

Event: SPIE Remote Sensing, 2018, Berlin, Germany

Development of a Mars lidar (MARLI) for measuring wind and aerosol profiles from orbit

Daniel R. Cremons[1,2], James Abshire[1], Graham Allan[1,3], Xiaoli Sun[1], Haris Riris[1], Michael Smith[1], Scott Guzewich[1], Anthony Yu[1], Floyd Hovis[4]

[1] NASA Goddard Space Flight Center, Greenbelt MD 20771; [2] Universities Space Research Association, Columbia MD 21046; [3] Sigma Space Corporation, Lanham MD 20706; [4] Fibertek Inc., Herndon VA 20171

ABSTRACT

Our understanding of the Mars atmosphere and the coupled atmospheric processes that drive its seasonal cycles is limited by a lack of observation data, particularly measurements that capture diurnal and seasonal variations on a global scale. As outlined in the 2011 Planetary Science Decadal Survey and the recent Mars Exploration Program Analysis Group (MEPAG) Goals Document, near-polar-orbital measurements of height-resolved aerosol backscatter and wind profiles are a high-priority for the scientific community and would be valuable science products as part of a next-generation orbital science package. To address these needs, we have designed and tested a breadboard version of a direct detection atmospheric wind lidar for Mars orbit. It uses a single-frequency, seeded Nd:YAG laser ring oscillator operating at 1064 nm (4 kHz repetition rate), with a 30-ns pulse duration amplified to 4 mJ pulse energy. The receiver uses a Fabry-Perot etalon as part of a dual-edge optical discrimination technique to isolate the Doppler-induced frequency shift of the backscattered photons. To detect weak aerosol backscatter profiles, the instrument uses a 4x4 photon-counting HgCdTe APD detector with a 7 MHz bandwidth and < 0.4 fW/Hz$^{1/2}$ noise equivalent power. With the MARLI lidar breadboard instrument, we were able to measure Doppler shifts continuously between 1 and 30 m/s by using a rotating chopper wheel to impart a Doppler shift to incident laser pulses. We then coupled the transmitter and receiver systems to a laser ranging telescope at the Goddard Geophysical and Astronomical Observatory (GGAO) to measure backscatter and Doppler wind profiles in the atmosphere from the ground. We measured a 5.3 ± 0.8 m/s wind speed from clouds in the planetary boundary layer at a range of 4 to 6 km. This measurement was confirmed with a range-over-time measurement to the same clouds as well as compared to EMC meteorological models. Here we describe the lidar approach and the breadboard instrument, and report some early results from ongoing field experiments.

Keywords: Mars, lidar, clouds, wind, Doppler, HgCdTe, aerosol

1. Introduction

Despite an increase in the quantity and quality of Mars atmospheric data from space-based instrumentation[1–5] – as well as the corresponding modeling efforts[6,7] – further progress will require new measurement capabilities, including those that target diurnal variations of aerosols, water vapor abundance, and wind velocity[8,9]. Despite the low atmospheric pressure, winds on Mars can raise large amounts of dust into the atmosphere; these winds are known to play a key role in volatile species and energy transport, though their seasonal, diurnal, and spatial behavior on the global scale are still largely unknown or poorly constrained[5,10,11]. Additionally, winds play a vital role in regulating the transfer of water vapor and heat throughout the atmosphere and are a primary factor in all surface-atmosphere interactions[12]. Dust particles interact strongly with infrared (IR) radiation causing large changes in the thermal structure and act as a driver of atmospheric motions at all spatial scales[13]. Observations show that the main variability in the present-day Mars climate is related to variations in the spatial and temporal distribution of dust and water ice aerosols[14,15], including the global dust events that blanket the planet during some Mars years[16]. The ability to measure wind across the Mars globe at all times of day and throughout seasons would directly impact science goals relating to tracking methane as a biomarker[17,18], and water vapor

Lidar Technologies, Techniques, and Measurements for Atmospheric Remote Sensing XIV
edited by Upendra N. Singh, Georgios D. Tzeremes, Proc. of SPIE Vol. 10791, 1079106
 · doi: 10.1117/12.2325408

which may end up in briny deposits[19–22]. Finally, dust storms and high winds affect current and future robotic and crewed mission operations on the surface that require consistent solar irradiation[23,24], as well as exploration using rotorcraft such as the Mars Helicopter Scout[25,26].

Here, we report the continued development and breadboard testing of a direct-detection Doppler wind lidar for Mars orbit (MARLI), which is being developed to provide 4D measurements of dust, water vapor, and wind globally, regardless of lighting conditions or season[27–30]. Due to the increased necessity of wind and aerosol measurements on Mars, the 2011 Planetary Science Decadal Survey and the Mars Exploration Program Analysis Group (MEPAG) Goals Documents have cited several investigation aims which could be directly addressed by wind measurements from orbit[9]:

- Measure the state and variability of the lower atmosphere from turbulent scales to global scales.
- Characterize dust, water vapor, and clouds in the lower atmosphere.
- Measure the forcings that control the dynamics and thermal structure of the lower atmosphere.
- Measure the turbulent fluxes of dust and volatiles between surface and atmospheric reservoirs.

As an orbital lidar, MARLI will also measure heights continuously, which can used to refine previous measurements, measure seasonal or annual changes in surface height, and co-locate aerosol measurements from lander and orbital volatile measurements. Due to Mars' low atmospheric pressure and the laser's near-IR wavelength, almost all atmospheric backscatter is from Mie scattering from aerosols. MARLI makes range-resolved measurements of atmospheric backscatter, which can be used to measure dust and depolarization (scattering from ice) as a function of altitude, location, and time. Finally, the dual-edge etalon approach is used to frequency resolve the aerosol backscatter to allow global wind measurements as a function of range along the instrument line-of-sight (LOS). Since all of these measurements come from the same instrument, the resulting dataset is self-consistent, which is a substantial benefit for subsequent analysis. The three measurement types are illustrated in Figure 1.

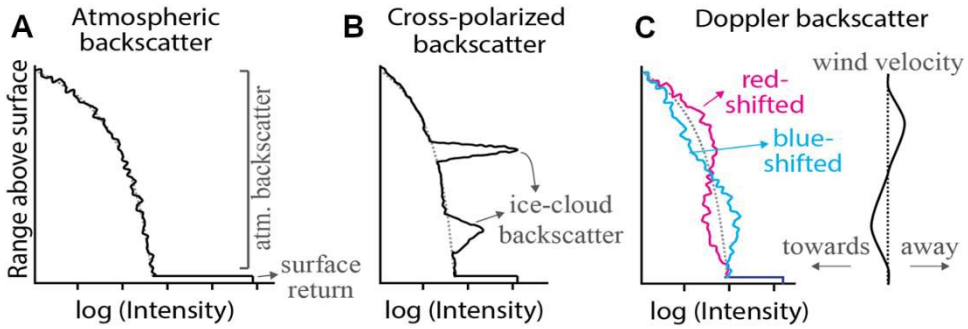

Figure 1. Illustration of measurements from the MARLI lidar. (**A**) Range-resolved aerosol backscatter and surface return. (**B**) Cloud height, thickness, and particle shape from cross-polarized return. (**C**) Range-resolved LOS wind measurements across the spacecraft track.

2. Instrument and Orbit Parameters

MARLI is designed for a nominally circular polar orbit at an altitude of approximately 400 km. The lidar design makes use of heritage from successful flight-proven planetary laser altimeters (LOLA, MOLA, MLA), with a single-frequency Nd:YAG laser based on that flow on the CATS lidar on ISS[31]. The flight instrument receiver will be a 60-cm Cassegrain telescope, similar to the ATLAS lidar for the upcoming ICESat-2 mission[32]. The detector is a 4x4 photon-counting HgCdTe avalanche photodiode (APD) with a 7 MHz bandwidth and < 0.4 fW/Hz$^{1/2}$ noise equivalent power[33–36]. Although the lidar will return information at a 10 Hz rate and 150-m vertical resolution, the summary in Table 1 is based on averaging into 2 km range bins and for 40 seconds along track (~2 deg in latitude).

Table 1. MARLI instrument parameters and nominal performance for a Mars polar orbit

Lidar Parameters		Mission Parameters	
Transmitter wavelength	1064 nm	Orbit altitude	400 km
Laser pulses/s	250	Off-nadir pointing angle	30°
Pulse energy	4 mJ	One-way transmission	0.7
Pulse width	25 ns	Diffuse surface reflectivity	0.26
Transmitter divergence	40 µrad	Atm. backscatter coeff. at 5 km	$3 \cdot 10^{-6}$ $m^{-1}sr^{-1}$
Telescope diam.	50 cm	Spatial averaging	2°
Receiver bandwidth	100 MHz	Averaging length	120 km
Receiver FOV	60 µrad	Atmospheric range bin	2 km
Detector quantum efficiency	75%	Backscatter SNR (0-25 km alt.)	150-30
Detector bandwidth	8 MHz	Wind speed std. dev (0-25 km alt.)	1.8-7.5 m/s

The current design is for the lidar pointing angle to be ~ 30 deg. cross-track, allowing for measurement of horizontal atmospheric wind from an orbiting spacecraft (Figure 2). A single transmitter/receiver system would enable a scalar wind measurement (*i.e.*, cross-track amplitude), while a dual-transmitter/receiver system, with two telescopes offset off-nadir 90 degrees from one another could allow a continuous vector wind measurement. An alternative vector measurement with coarser spatial resolution may also be accomplished with a single, gimballed lidar that rotates the off-axis angle. This approach is being considered as an implementation option.

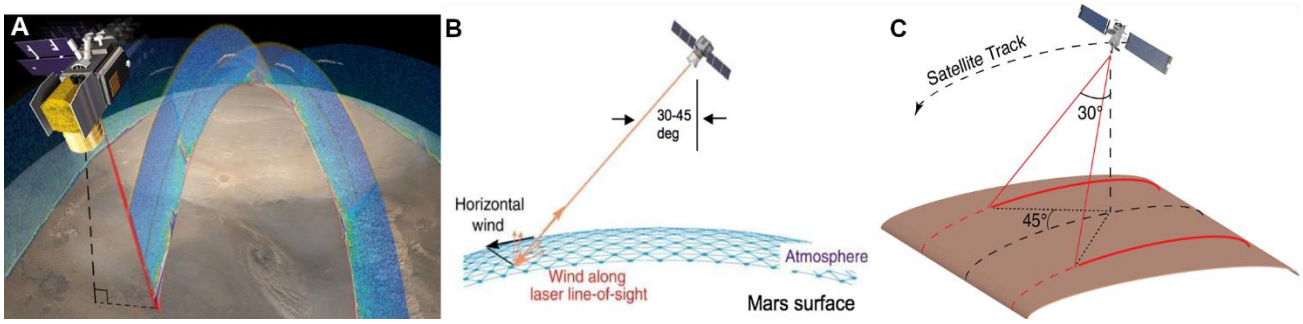

Figure 2. MARLI measurement concept. (**A**) Conceptual drawings of the MARLI instrument in a Mars polar orbit. (**B**) Off-nadir measurement concept for scalar wind measurement along lidar line-of-sight (LOS). (**C**) A dual-beam concept of the instrument, which allows vector wind measurements.

In order to measure aerosol motion with respect to the laser transmitter LOS, MARLI has an optical frequency discriminator based on a dual-edge etalon technique[37]. Briefly, the atmospherically-backscattered laser energy that is collected by the receiver telescope is split into two paths, which are directed through a solid, fused-silica etalon (50-mm diameter, 40-mm thickness, FSR: 2.59 GHz) at two different angles. One is normally incident and the other is offset by 1.2 mrad from normal. This angular offset shifts the optical passband of the etalon for one of its peaks with respect to the other, forming a double-edge frequency discriminator (Figure 3A). The ratio of the difference over the sum (RDoS) of the transmission of the two filters produces a gradient as function of Doppler shift (Figure 3B). Locking of the seed-laser frequency at the crossing point of the two peaks places the zero-shift point at the maximum of the filter gradient, enabling a sensitive Doppler measurement. Mars' low atmospheric pressure and high aerosol content allows use of the fundamental laser emission at 1.064 µm, in contrast to approaches for measuring winds in the Earth's atmosphere that use the laser's second or third harmonic wavelengths[38,39].

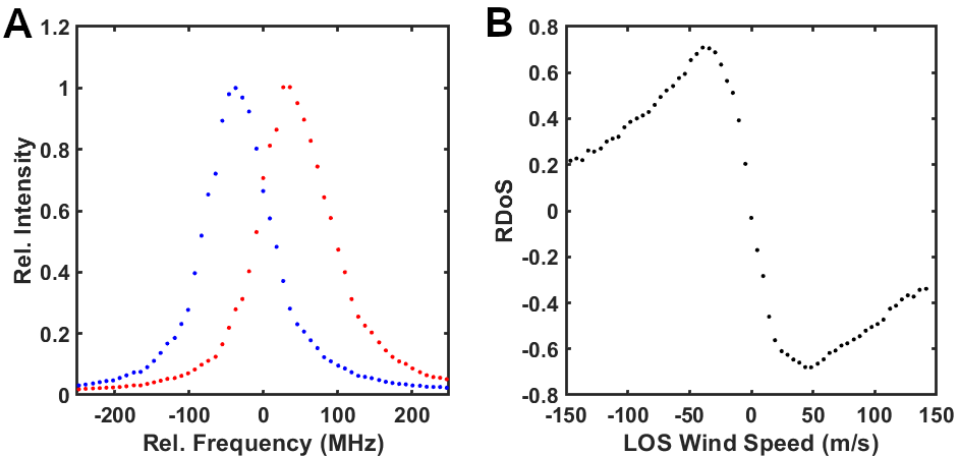

Figure 3. **Double-edge Doppler discriminator** (**A**) the measured pass-bands of the breadboard lidar's etalon. Intensity has been normalized to the maximum height of the higher peak. The frequency has been offset to the crossing point of the two pass bands. (**B**) Ratio of the difference over the sum (RDOS) from (**A**) showing the Doppler measurement's response versus wind velocity parallel to the line of sight (LOS). The laser frequency is set at the crossing-point from (**A**), which is 281.625692 THz.

3. Laboratory Doppler Experiments

The breadboard Doppler discriminator subsystem that we constructed is shown in Figure 4. The backscattered light is directed from the telescope (or introduced via multi-mode optical fiber, as shown here), and is collimated by a plano-convex lens to < 0.7 mrad divergence. The collimated beam is then split into two beams of equal intensity by a 50:50 cube beam-splitter (center, top). The two lines (Figure 4, red and blue) are directed through the solid etalon, offset ~1.2 mrad from one another. Due to the temperature dependence of the index of refraction, the fused-silica etalon's pass bands tune with temperature. To minimize the shift, we housed the etalon in a thermally-insulated enclosure, which has a 25-W internal heating element and uses a small, air-circulating fan to create a stable temperature bath. The transmitted beams are then directed through daylight-blocking filters before being focused by 100-mm FL plano-convex lenses into a twin-core, multi-mode fiber, which directs the light to the HgCdTe APD detector system.

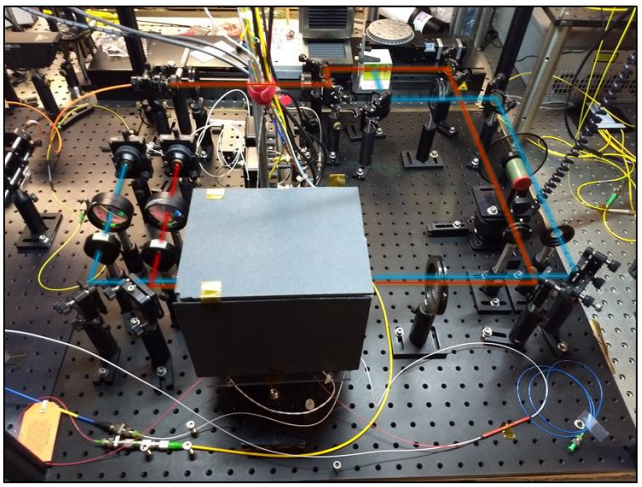

Figure 4. **Layout of the breadboard etalon discriminator subsystem in the laboratory.** The red and blue beams represent the two receiver paths that are transmitted through the etalon (large grey box in foreground) at slightly different angles. The received light from the telescope enters the module in the upper left (orange optical fiber) and exits in the middle left (end of blue and red beams). The system is shown in the fiber-coupled setup, which is used for alignment and calibration. The black aluminum breadboard on which the module is contained is 61x91 cm.

To demonstrate measurements with the MARLI breadboard, we coupled the dual-beam etalon module to the Nd:YAG laser transmitter and the HgCdTe APD detector (Figure 5). We first simulated a Doppler signal by focusing the transmitted laser onto an optical chopping wheel that was mounted at a 60° angle with respect to the incident laser pulses. By rotating the chopping wheel at various frequencies, we simulated wind speeds from 0.8 to 30.3 m/s. The light scattered from the optical chopper was collected and collimated with a plano-convex lens and, as in Figure 4, split into two beams that were passed through the etalon at a 1.2-mrad angular difference from one another. The beams were focusing into the two cores of a twin-core, multimode optical fiber, which coupled the optical signals from each path (henceforth denoted CH0 and CH1) onto separate pixels of the detector focal plane array. In order to protect the optical elements and the detector, the pulse energy of the laser incident on the chopping wheel was reduced to 4 µJ.

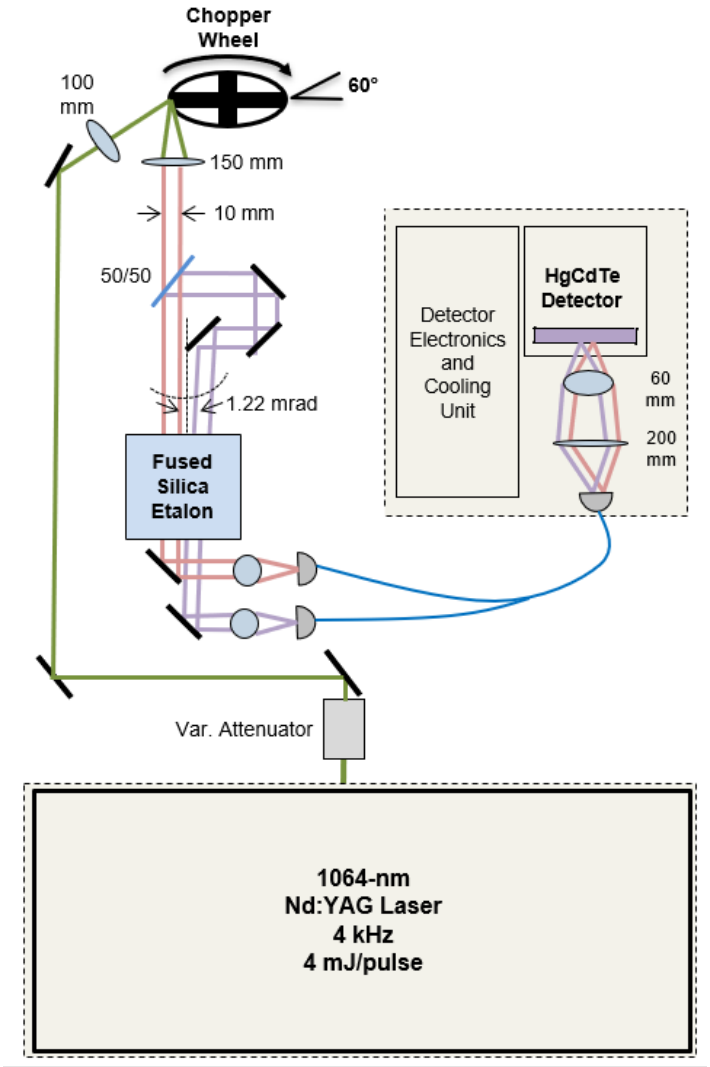

Figure 5. Laboratory experiment to measure Doppler shifts using the MARLI breadboard. The green lines represent the laser path from the laser head to the Doppler-shift-imparting optical chopper. The chopper in the schematic is seen face-on but is actually tilted 40° with respect to the incident laser pulses, which causes a red-shift of the backscattered photons. The red and purple lines represent the two beams (*i.e.*, dual-edge filters) which are transmitted through the etalon at a 1.2-mrad angular difference. The blue lines represent the dual-core optical fiber which routes the filtered light from the etalon to the HgCdTe focal plane array detector, where the two beams are focused onto separate pixels of the 4x4 pixel array.

The results of the laboratory Doppler measurements are shown in Figures 6 and 7. First, the transmission of the etalon was measured for the two channels as a function of frequency, as shown in Figure 2A, and the seed-laser frequency was locked at the maximum of the gradient. The laser frequency was continuously monitored with a high-precision wavelength meter (HighFinesse Laser and Electronics Systems GmbH), and was corrected via piezoelectric tuning if the laser frequency deviated by more than 5 MHz from the setpoint. The chopper rotational frequency was then changed as a function of time (Figure 6A), and the APD voltages from the pixels corresponding to CH0 and CH1 were recorded at a 120 MHz sample rate. The voltage from each optical pulse on the detector was isolated in time and averaged with subsequent pulse over a 100-ms duration. The RDoS of the two channels was then calculated, and is displayed as a function of time in Figure 6B. The RDoS captures changes the chopper speed well between 30 and 1 m/s.

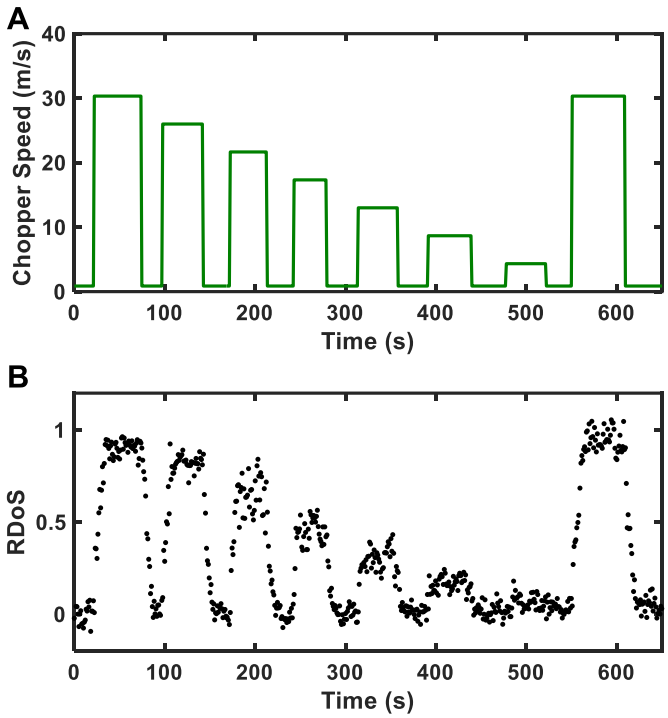

Figure 6. Results from the laboratory experiment, showing the frequency discrimination using backscatter from optical chopping wheel at various frequencies. (**A**) Chopper speed as calculated from rotational frequency and incident laser angle as a function of time. (**B**) Ratio of the difference over the sum (RDoS) as a function of time for the same period as (**A**). The points shown represent a 1-s average.

Following this preliminary experiment, the optical chopper was run at a low frequency (20 Hz; 0.86 m/s) to obtain a low-Doppler-shift measurement for 50 seconds, then the chopper frequency was increased to 700 Hz, corresponding to a simulated 30.3 m/s wind, for 40 seconds. The voltages of two pixels of the HgCdTe APD were measured by a 12-bit ADC and a National Instruments FPGA module running at 120 MS/s. As can be seen in Figure 7, the change in chopper speed corresponds to a drop in the CH0 voltage and a rise in the CH1 voltage as the chopper imparts an increasing blue shift to the laser pulses as it accelerates to 700 Hz. Ten seconds after the chopper frequency command is sent, the optical chopper reaches 700 Hz and the voltages begin to stabilize at their new values. The low-frequency (0.1 Hz) oscillations seen in the CH1 signal at high rotational frequency are due to the chopper wheel wobble (*i.e.*, slight change in the angle at which pulses scatter off of the chopper and are collimated) at the rotational frequency of 700 Hz. The change in voltage of each channel results in an overall drop in the RDoS as a function of Doppler shift. The change in RDoS from -0.05 to -0.62 for a 30 m/s change in Doppler shift corresponds to a 7% change in signal per m/s of velocity. Figure 7B shows the successful results of the laboratory test of the MARLI breadboard system using an optical chopper to impart a Doppler shift. For the low speed (0.86 m/s) time frame, the measured chopper speed was 0.2 ± 0.1 m/s over the 50-s measurement window. For the 30.3 m/s simulated wind speed, the measured chopper speed was 29 ± 1 m/s, though the standard deviation is large here due to the low frequency signal oscillations caused by the chopper blade wobbling.

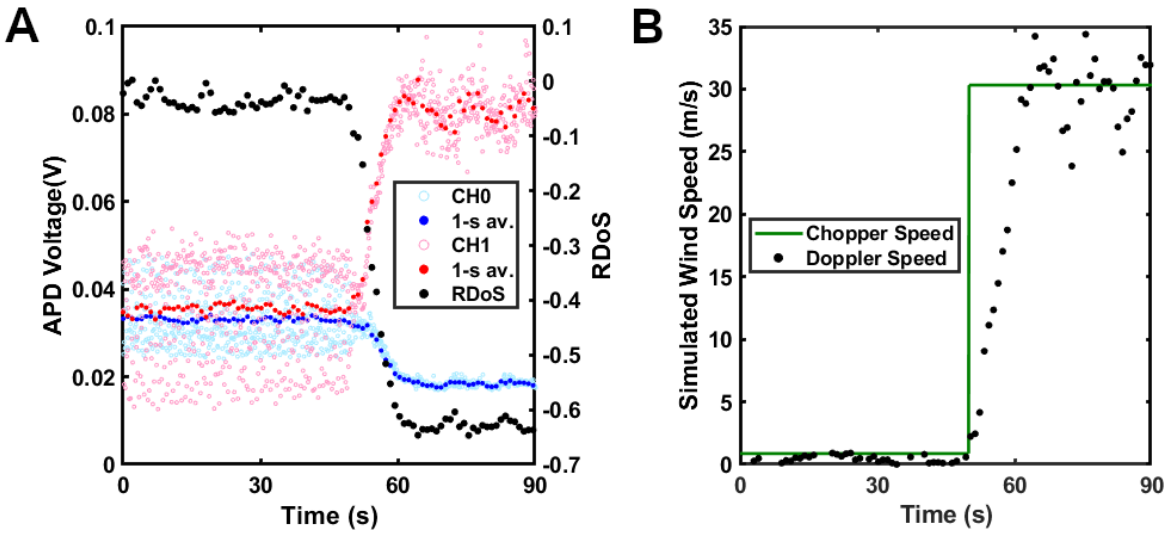

Figure 7. Demonstration of Doppler discrimination using full MARLI laboratory setup. (**A**) HgCdTe APD voltage as a function of time for each of the two filter channels (CH0 and CH1). The light blue dots represent the 100-ms integration time for channel 0, and the dark blue dots represent the 1-s average of the light blue dots. Similarly, the pink dots represent the 100-ms integration time for channel 1, and the dark red dots represent the 1-s average of the pink dots. The black dots are the RDoS of the 1-s averaged points from CH0 and CH1 as a function of time. (**B**) The calculated chopper speed calculated from the Doppler shift of the backscattered laser pulses as a function of time along with the corresponding optical chopper speed. The chopper speed is calculated from the rotational frequency of the wheel, the wheel diameter, and the incident laser angle.

4. Status of Field Experiments and Initial Wind Measurements

The next step in the MARLI development was a campaign to demonstrate wind measurements in the open atmosphere. The 1.2-m laser ranging telescope at the Goddard Geophysical and Astronomical Observatory (GGAO) in Beltsville, MD was selected for its proximity to Goddard Space Flight Center and full azimuthal range. In addition, the large aperture size allowed expansion of the transmitted beam to an eye-safe size. Despite the large collecting area, the transmitter-receiver overlap was small due to the constraints of this particular telescope. As stated above, the MARLI instrument will use a 50-cm receiver to achieve the stated wind measurements in Table 1. Atmospheric tests from Earth's surface have significantly different conditions (aerosol density, atmospheric pressure, solar background noise, thermal stability, *etc.*) than for an orbital instrument for Mars, but they are important to demonstrate the lidar measurement approach. The laser, discriminator module, detector, and accompanying electronics were transported to the field site, after which we performed setup, alignment of the system, and software development. An overview of the field experiments, including the telescope and breadboard instrument are shown in Figure 8. To ensure eye-safe conditions for the beam leaving the telescope, the transmitter beam was expanded to 22-cm diameter and the laser pulse energy was kept below 300 µJ.

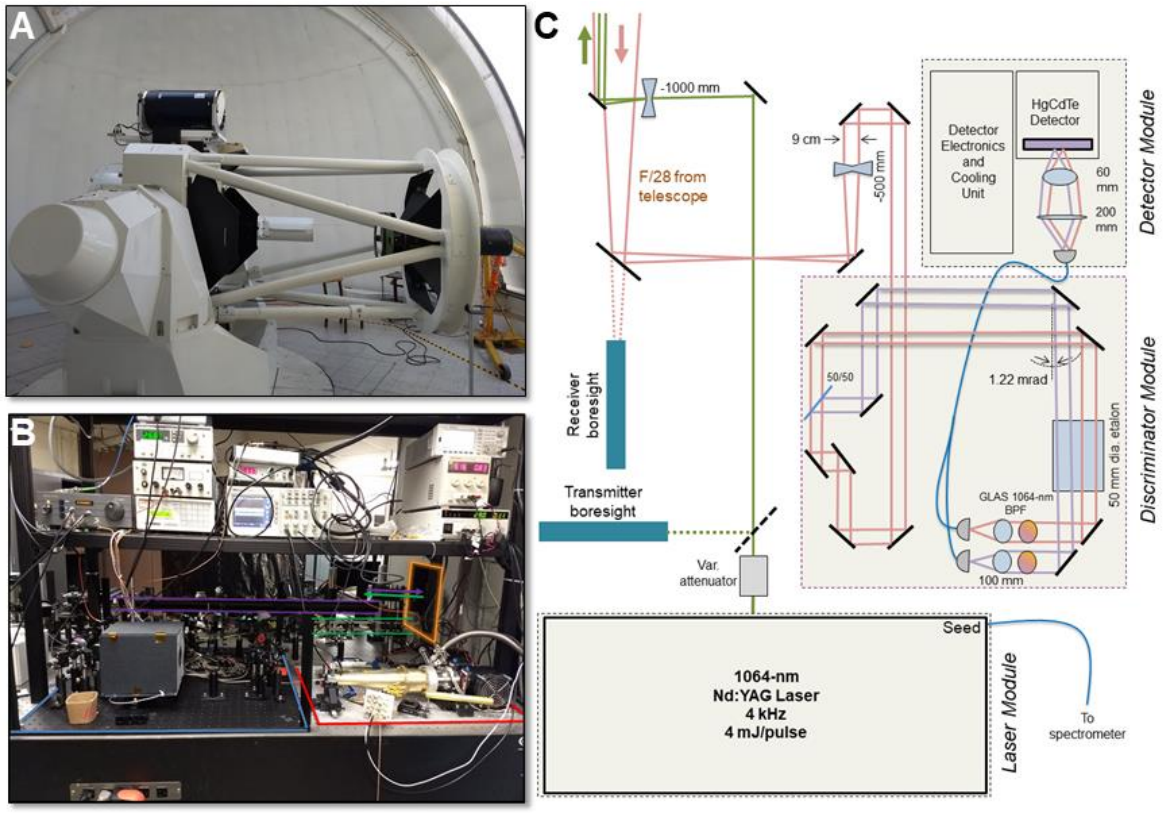

Figure 8. Field experiment's setup at the Goddard Geophysical and Astronomical Observatory's 1.2-m telescope. (**A**) The 1.2-m Coudé telescope. (**B**) Breadboard instrument on site at GGAO. The region outlined in blue is the discriminator module (compare to figure 4). The region outlines in red is the detector module including electronics and cooling system. The purple lines correspond to the transmission path, and the green lines correspond to the receiver path. The orange frame in the upper right is the port to the first mirror of the 5-mirror Coudé system. (**C**) Schematic of MARLI breadboard for field experiments at the Goddard Geophysical and Astronomical Observatory. The green lines correspond to the transmitter laser light, the red lines correspond to the received light, which is then split into two beams, shown in purple and red, to be passed through the etalon. The blue lines correspond to optical fiber.

The initial efforts focused on aligning the transmitter and receiver paths to maximize overlap at 2-5 km range, corresponding to high concentrations of aerosols around the planetary boundary layer. Tests to optimize the transmission beam-divergence were performed, which resulted in strong return signals from aerosols at ranges up to 12 km. Figure 9 shows a sample of the cloud ranging experiments that were made with modified receiver optics that bypasses the discriminator module. Variations in the cloud altitude with time can be observed, as well as multiple cloud layers and shapes. The ADC used to record the signal from the HgCdTe APD was triggered by each transmitted laser pulse and recorded in 120-μs intervals at 66-ns steps, corresponding to 10-m in range per bin.

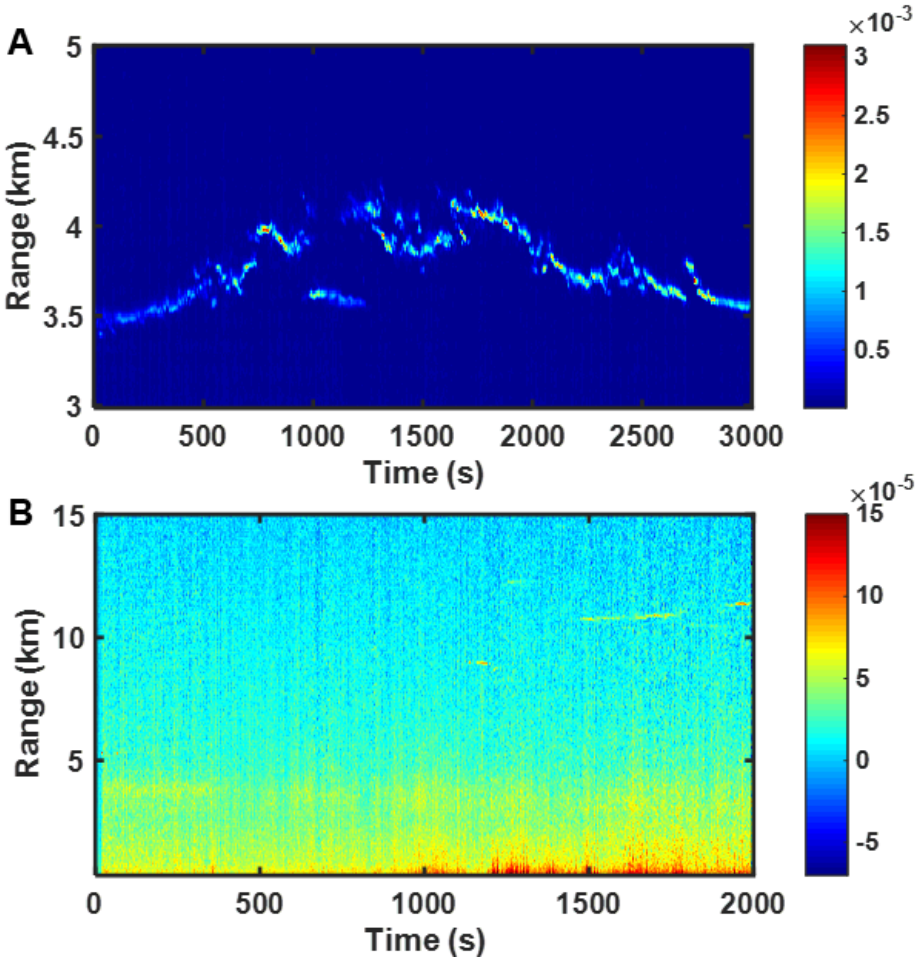

Figure 9. **Some results from measuring atmospheric backscatter with the MARLI field experiment**. (**A**) Cloud returns from 3 to 5 km range as a function of experimental time. (**B**) Cloud ranging to high-altitude clouds at 12 km range. The color scale corresponds to voltage from the HgCdTe APD.

To perform atmospheric wind measurements, we coupled the optical path from the 1.2-m telescope to the discriminator subsystem, as shown in Figure 9. The laser pulse energy was attenuated to 300 uJ, and the telescope azimuth was set to match the wind direction (here, due west). The telescope's elevation was set to 25°, which resulted in 90% of the horizontal wind speed to be imparted to the backscattered photons. The bias of the HgCdTe APD was set to 12 V, corresponding to a gain of more than 300[33]. The etalon was characterized in the same method as in Figure 2, which we used to generate a lookup table (LUT) for wind measurements from the measured RDoS values. The seed laser was locked to the crossing point of the two filters to ensure that a zero Doppler shift corresponded to a zero RDoS. This was verified by recording the backscatter return from surfaces within the telescope (*i.e.*, zero-range backscatter). Figure 10 shows wind measurements from clouds at 4 to 6-km range (2-km altitude).

A moving average of two bins (120-ns) was performed on each 120-µs record. In addition, a moving average of 10-s was performed on the entire experimental set. Post-processing also included a baseline subtraction, as well as noise filtering based on the long-range signal variance. This noise filtering involved calculating the signal variance from the farthest range portion (from 17 to 18 km range), within which the signal is background-noise limited and below the noise level. From this, any background-subtracted voltages that are over twice the variance of that signal are preserved, and values below are set to zero signal and zero wind. Figure 10A and 10B show the range-resolved backscatter profiles from CH0 and CH1 respectively as a function of time. The pixel-by-pixel RDoS was calculated using the averaged dataset, and is shown in Figure 10C. The same cloud features can be seen in the RDoS plot as in the backscatter plots (Figure 10A and

B), with the strongest scattering features exhibiting an RDoS value near 0.2. A positive RDoS indicates a blue-shift due to aerosol scattering. The RDoS values were then run through the LUT generated from etalon characterization performed prior to the start of the experiment.

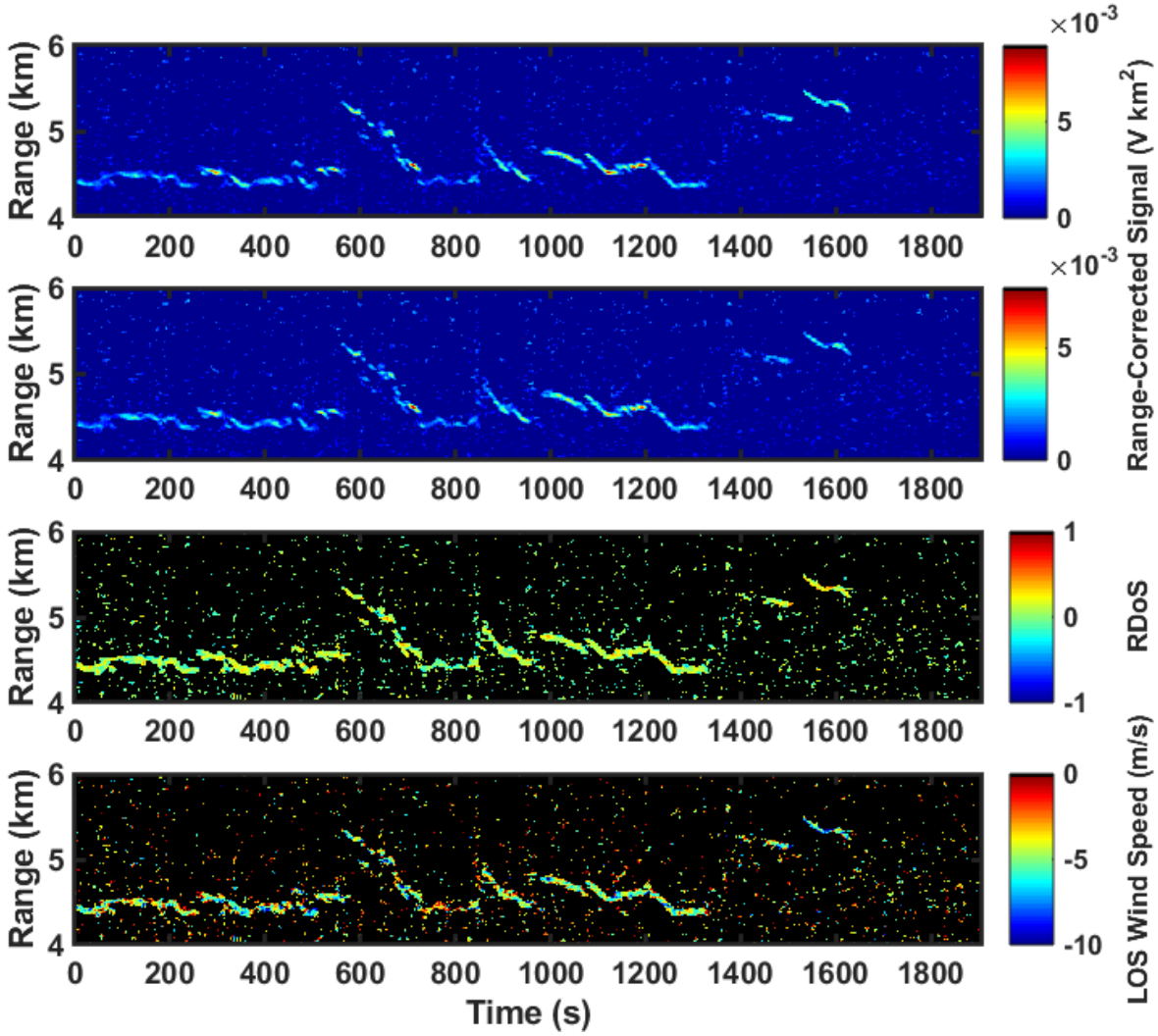

Figure 10. **Initial results from MARLI field experiments.** (**A, B**) Range-resolved backscatter signal as a function of experimental time for CH0 and CH1, respectively. The colorbar corresponds to APD voltage, with warmer colors corresponding to higher voltage, and cooler colors corresponding to lower voltage. The data shown here are a moving average of 2 range bins and 41,000 consecutive 120-μs periods, collated by range bin, for a 10-s moving average in the Time direction. (**C**) The ratio of the difference over the sum for CH0 and CH1 as a function of time from (**A**) and (**B**). The colorbar represents the RDoS value, with cooler colors corresponding to a negative RDoS (*i.e.*, red shift), and warmer colors to a positive RDoS (*i.e.*, blue shift). All values excluded via the noise filter have been set to an RDoS of 1. (**D**) LOS wind values generated from the etalon pass-band LUT and the corresponding RDoS values for each pixel. The colorbar represents wind speed, with cooler colors corresponding to a higher wind speed towards the telescope, and warmer colors representing a lower wind speed towards the telescope. All four panels show the same portions of range and time.

The extracted wind measurements from the cloud baskscatter are shown in Figure 10D. The wind values are all negative, which corresponds to the observed blue shift due to the telescope being pointed upwind. The values from the clouds are all between 0 and -10 m/s, with the highest SNR regions (for example, between 800s and 1000s) yielding a value of -5.3 ± 0.8 m/s for a 60-s, 200-m range average. The negatively-sloped diagonal features resulting from cloud backscatter as a function of range and time confirm that the telescope was pointed upwind. Based on the range/time gradient from the cloud feature from 580 s to 700s, a cloud velocity of -4.6 m/s was measured, which is in close agreement with the Doppler measurement of -5.3 m/s. We note that the cloud ranging measurement here allows for a validation of

the Doppler measurements, but is only possible due to the discrete cloud features present in our earth-based measurements. In the Mars atmosphere the vast majority of measurements will be from more uniformly distributed aerosols, which will preclude extraction of a wind measurement from simple ranging and necessitating the Doppler technique. Both wind measurements (Doppler and range/time) are in line with the wind values (5.9 m/s from the West) for the date, time, and altitude from the Environmental Modeling Center Global Forecast System.

5. Summary and Future Work

We have described our approach and status of breadboard experiments for a direct detection wind and aerosol lidar that we are developing for Mars orbit. Global wind measurements and constraints on aerosol concentrations (H_2O, dust, and CO_2) in the Mars atmosphere as a function of latitude and season are high-priority measurement objectives for future Mars missions. The MARLI approach will allow wind measurements from a 400-km polar orbit with 150-m range bins and a 10-Hz data rate. Designs for both scalar and vector wind measurement capabilities were described. In development to date we have performed simulated wind measurements in the laboratory using an optical chopper wheel, which demonstrate the measurement concept. We then performed field experiments at the Goddard Geophysical and Astronomical Observatory using a ground-based 1.2-m telescope, and have obtained preliminary wind measurements from clouds in the planetary boundary layer of 5.3 ± 0.8 m/s. at range of 4 km. Our field experiments are ongoing with the objective to measure Doppler shifts with weaker signals. We have also begun work on the key elements of a brassboard instrument with the objective of bringing the key elements to TRL-6 by the end of 2019.

References

[1] Holstein-Rathlou, C., Gunnlaugsson, H. P., Merrison, J. P., Bean, K. M., Cantor, B. A., Davis, J. A., Davy, R., Drake, N. B., Ellehoj, M. D., Goetz, W., Hviid, S. F., Lange, C. F., Larsen, S. E., Lemmon, M. T., Madsen, M. B., Malin, M., Moores, J. E., Nørnberg, P., Smith, P., et al., "Winds at the phoenix landing site," J. Geophys. Res. E Planets **115**(E5), E00E18 (2010).

[2] Desai, P. N., Prince, J. L., Queen, E. M., Schoenenberger, M. M., Cruz, J. R. and Grover, M. R., "Entry, Descent, and Landing Performance of the Mars Phoenix Lander," J. Spacecr. Rockets **48(**5), 798–808 (2011).

[3] Madeleine, J. B., Forget, F., Millour, E., Montabone, L. and Wolff, M. J., "Revisiting the radiative impact of dust on Mars using the LMD Global Climate Model," J. Geophys. Res. Planets **116**(E11), E11010 (2011).

[4] McCleese, D. J., Heavens, N. G., Schofield, J. T., Abdou, W. A., Bandfield, J. L., Calcutt, S. B., Irwin, P. G. J., Kass, D. M., Kleinböhl, A., Lewis, S. R., Paige, D. A., Read, P. L., Richardson, M. I., Shirley, J. H., Taylor, F. W., Teanby, N. and Zurek, R. W., "Structure and dynamics of the Martian lower and middle atmosphere as observed by the Mars Climate Sounder: Seasonal variations in zonal mean temperature, dust, and water ice aerosols," J. Geophys. Res. **115(**E12), E12016 (2010).

[5] Smith, M. D., "Spacecraft Observations of the Martian Atmosphere," Annu. Rev. Earth Planet. Sci. **36**, 191–219 (2008).

[6] Lee, C., Richardson, M. I., Mischna, M. A. and Newman, C. E., "Realistic dust and water cycles in the MarsWRF GCM using coupled two-moment microphysics," Am. Astron. Soc. DPS Meet. #49 (2017).

[7] Segura, T. L., Toon, O. B. and Colaprete, A., "Modeling the environmental effects of moderate-sized impacts on Mars," J. Geophys. Res. Planets **113**(E11), E11007 (2008).

[8] Heavens, N. G., Benson, J. L., Kass, D. M., Kleinböhl, A., Abdou, W. A., McCleese, D. J., Richardson, M. I., Schofield, J. T., Shirley, J. H. and Wolkenberg, P. M., "Water ice clouds over the Martian tropics during northern summer," Geophys. Res. Lett. **37**(18), L18202 (2010).

[9] Hamilton, V. E., "Mars Science Goals, Objectives, Investigations, and Priorities: 2015" (2015).

[10] Greeley, R. and Thompson, S. D., "Mars: Aeolian features and wind predictions at the Terra Meridiani and Isidis Planitia potential Mars Exploration Rover landing sites," J. Geophys. Res. **108**(E12) (2003).

[11] Kahn, R., "The spatial and seasonal distributions of Martian clouds and some meteorological implications," J. Geophys. Res. **89**(A8), 6671–6688 (1984).

[12] Clancy, R. T., Grossman, A. W., Wolff, M. J., James, P. B., Rudy, D. J., Billawala, Y. N., Sandor, B. J., Lee, S. W. and Muhleman, D. O., "Water vapor saturation at low altitudes around Mars aphelion: A key to Mars climate?," Icarus **122**(1), 36–62 (1996).

[13] Gierasch, P. J. and Goody, R. M., "The Effect of Dust on the Temperature of the Martian Atmosphere," J. Atmos. Sci. **29**(2), 400–402 (1972).

[14] Smith, M. D., "Interannual variability in TES atmospheric observations of Mars during 1999–2003," Icarus **167**(1), 148–165 (2004).

[15] Read, P. L., Lewis, S. R. and Mulholland, D. P., "The physics of Martian weather and climate: a review," Reports Prog. Phys. **78**(12), 125901 (2015).

[16] Wang, H. and Richardson, M., "The origin, evolution, and trajectory of large dust storms on Mars during Mars years 24–30 (1999–2011)," Icarus **251**, 112–127 (2015).

[17] Mischna, M. A., Allen, M., Richardson, M. I., Newman, C. E. and Toigo, A. D., "Atmospheric modeling of Mars methane surface releases," Planet. Space Sci. **59**(2–3), 223–237 (2011).

[18] Krasnopolsky, V. A., Maillard, J. P. and Owen, T. C., "Detection of methane in the martian atmosphere: evidence for life?," Icarus **172**(2), 537–547 (2004).

[19] Chevrier, V. F. and Rivera-Valentin, E. G., "Formation of recurring slope lineae by liquid brines on present-day Mars," Geophys. Res. Lett. **39**(21), L21202 (2012).

[20] McEwen, A. S., Dundas, C. M., Mattson, S. S., Toigo, A. D., Ojha, L., Wray, J. J., Chojnacki, M., Byrne, S., Murchie, S. L. and Thomas, N., "Recurring slope lineae in equatorial regions of Mars," Nat. Geosci. **7**, 53 (2013).

[21] Ojha, L., Wilhelm, M., Murchie, S., McEwen, A. S., Wray, J. J., Hanely, J., Masse, M. and Chojnacki, M., "Spectral evidence for hydrated salts in recurring slope lineae on Mars," Nat. Geosci. **8**, 829–932 (2015).

[22] Orosei, R., Lauro, S. E., Pettinelli, E., Cicchetti, A., Coradini, M., Cosciotti, B., Di Paolo, F., Flamini, E., Mattei, E., Pajola, M., Soldovieri, F., Cartacci, M., Cassenti, F., Frigeri, A., Giuppi, S., Martufi, R., Masdea, A., Mitri, G., Nenna, C., et al., "Radar evidence of subglacial liquid water on Mars," Science **361**, 490–493 (2018).

[23] Toigo, A. D., Richardson, M. I., Wang, H., Guzewich, S. D. and Newman, C. E., "The cascade from local to global dust storms on Mars: Temporal and spatial thresholds on thermal and dynamical feedback," Icarus **302**, 514–536 (2018).

[24] Cantor, B. A., "MOC observations of the 2001 Mars planet-encircling dust storm," Icarus **186**(1), 60–96 (2007).

[25] Grip, H., Johnson, W., Malpica, C., Scharf, D. P., Mandic, M., Young, L., Allan, B., Mettler, B. and San Martin, M., "Flight dynamics of a Mars Helicopter," Proc. Eur. Rotorcr. Forum (2017).

[26] Grip, H. F., Scharf, D. P., Malpica, C., Johnson, W., Mandic, M., Singh, G., Young, L. and Allan, B., "Guidance and Control for a Mars Helicopter," AIAA Guid. Navig. Control Conf. (2018).

[27] Abshire, J., Smith, M., Riris, H., Sun, X., Gentry, B. M., Yu, A. and Allan, G. R., "MARLI: MARs LIdar for global wind profiles from orbit," Eur. Planet. Sci. Congr. 2015 (2015).

[28] Guzewich, S., Abshire, J., Smith, M. D., Riris, H., Sun, X., Gentry, B. M., Yu, A. and Allan, G. R., "MARLI: MARs LIdar for global wind profiles from orbit," 47th Lunar Planet. Sci. Conf., 1497 (2016).

[29] Abshire, J., Guzewich, S., Smith, M., Riris, H., Sun, X., Gentry, B. M., Yu, A. and Allan., "MARLI: MARs LIdar for global wind profiles and aerosol profiles from orbit," 3rd Int. Work. Instrum. Planet. Mission. (2016).

[30] Abshire, J., Guzewich, S., Smith, M., Riris, H. and Allan, G. R., "Observations of Planetary Atmospheric Winds and Gases with Lidar," Planet. Sci. Vis. 2050 Work., 8102 (2017).

[31] Chuang, T., Burns, P., Walters, E. B., Wysocki, T., Deely, T., Losse, A., Le, K., Drumheller, B., Schum, T., Hart, M., Puffenburger, K., Ziegler, B. and Hovis, F., "Space-based, multi-wavelength solid-state lasers for NASA's Cloud Aerosol Transport System for International Space Station (CATS-ISS)," Proc. SPIE, Solid State Lasers XXII Technol. Devices **8599**, W. A. Clarkson and R. Shori, Eds., 85990N, International Society for Optics and Photonics (2013).

[32] Markus, T., Neumann, T., Martino, A., Abdalati, W., Brunt, K., Csatho, B., Farrell, S., Fricker, H., Gardner, A., Harding, D., Jasinski, M., Kwok, R., Magruder, L., Lubin, D., Luthcke, S., Morison, J., Nelson, R., Neuenschwander, A., Palm, S., et al., "The Ice, Cloud, and land Elevation Satellite-2 (ICESat-2): Science requirements, concept, and implementation," Remote Sens. Environ. **190**, 260–273 (2017).

[33] Beck, J., Welch, T., Mitra, P., Reiff, K., Sun, X. and Abshire, J., "A highly sensitive multi-element HgCdTe e-APD detector for IPDA lidar applications," J. Electron. Mater. **43**(8), 2910–2977 (2014).

[34] Sun, X., Abshire, J., Beck, J., Mitra, P., Reiff, K. and Yang, G., "HgCdTe avalanche photodiode detectors for airborne and spaceborne lidar at infrared wavelengths," Opt. Express **25**(14), 16589–16602 (2017).

[35] Beck, J., Wan, C., Kinch, M., Robinson, J., Mitra, P., Scritchfield, R., Ma, F. and Campbell, J., "The HgCdTe electron avalanche photodiode," J. Electron. Mater. **35**(6), 1166–1173 (2006).

[36] Sun, X., Abshire, J. B. and Beck, J. D., "HgCdTe e-APD detector arrays with single photon sensitivity for space lidar applications," SPIE Sens. Technol. + Appl., 91140K (2014).

[37] Flesia, C. and Korb, C. L., "Theory of the double-edge molecular technique for Doppler lidar wind measurement," Appl. Opt. **38**(3), 432–440 (1999).

[38] Durand, Y., Chinal, E., Endemann, M., Meynart, R., Reitebuch, O. and Treichel, R., "ALADIN airborne demonstrator: a Doppler Wind lidar to prepare ESA's ADM-Aeolus Explorer mission," SPIE Opt. + Photonics **6296**, 62961D (2006).

[39] Reitebuch, O., Lemmerz, C., Nagel, E., Paffrath, U., Durand, Y., Endemann, M., Fabre, F. and Chaloupy, M., "The Airborne Demonstrator for the Direct-Detection Doppler Wind Lidar ALADIN on ADM-Aeolus. Part I: Instrument Design and Comparison to Satellite Instrument," J. Atmos. Ocean. Technol. **26**(12), 2501–2515 (2009).